THE PHOTOGRAMMETRIC RECORD

The Photogrammetric Record 34(168): 385–407 (December 2019)

DOI: 10.1111/phor.12300

HYPERSPECTRAL OUTCROP MODELS FOR PALAEOSEISMIC STUDIES

Moritz Kirsch* (m.kirsch@hzdr.de)
Sandra Lorenz (s.lorenz@hzdr.de)
Robert Zimmermann (r.zimmermann@hzdr.de)
Louis Andreani (l.andreani@hzdr.de)
Laura Tusa (l.tusa@hzdr.de)
Solveig Pospiech (s.pospiech@hzdr.de)
Robert Jackisch (r.jackisch@hzdr.de)
Mahdi Khodadadzadeh (m.khodadadzadeh@hzdr.de)
Pedram Ghamisi (p.ghamisi@hzdr.de)
Gabriel Unger[1] (gabriel.unger@smul.sachsen.de)
Philip Hödl[2] (philip.hoedl@t-online.de)
Richard Gloaguen (r.gloaguen@hzdr.de)
Helmholtz Institute Freiberg for Resource Technology, Freiberg, Germany

Maarit Middleton (maarit.middleton@gtk.fi)
Raimo Sutinen (raimo.sutinen@gtk.fi)
Geological Survey of Finland, Rovaniemi, Finland

Antti Ojala (antti.ojala@gtk.fi)
Jussi Mattila[3] (jussi.mattila@rmcf.fi)
Nicklas Nordbäck (nicklas.nordback@gtk.fi)
Jukka-Pekka Palmu (jukka-pekka.palmu@gtk.fi)
Mia Tiljander (mia.tiljander@gtk.fi)
Timo Ruskeeniemi (timo.ruskeeniemi@gtk.fi)
Geological Survey of Finland, Espoo, Finland

**Corresponding author*
[1]*Sächsisches Landesamt für Umwelt,Landwirtschaft und Geologie, Freiberg, Germany*
[2]*Zentrum für Geoinformationswesen der Bundeswehr, Euskirchen, Germany*
[3]*Rock Mechanics Consulting Finland Oy, Vantaa, Finland*

Abstract

The traditional study of palaeoseismic trenches, involving logging, stratigraphic and structural interpretation, can be time consuming and affected by

biases and inaccuracies. To overcome these limitations, a new workflow is presented that integrates infrared hyperspectral and photogrammetric data to support field-based palaeoseismic observations. As a case study, this method is applied on two palaeoseismic trenches excavated across a post-glacial fault scarp in northern Finnish Lapland. The hyperspectral imagery (HSI) is geometrically and radiometrically corrected, processed using established image processing algorithms and machine learning approaches, and co-registered to a structure-from-motion point cloud. HSI-enhanced virtual outcrop models are a useful complement to palaeoseismic field studies as they not only provide an intuitive visualisation of the outcrop and a versatile data archive, but also enable an unbiased assessment of the mineralogical composition of lithologic units and a semi-automatic delineation of contacts and deformational structures in a 3D virtual environment.

Keywords: geology, hyperspectral imaging, outcrop models, palaeoseismology, remote sensing, SfM photogrammetry

Introduction

Palaeoseismology uses evidence from earthquakes preserved in the geologic and geomorphic record to reconstruct the seismic history of a fault system and assess the seismic hazard of a region. A common technique in palaeoseismological investigations is to excavate trenches on fault scarps (McCalpin, 2009). The documentation of palaeoseismic deformation features of lithologic units exposed in trenches is traditionally accomplished by *in situ* field mapping and/or by photomosaic logging (Rockwell and Ben-Zion, 2007; Lacan et al., 2018). These methods are prone to certain biases and errors that may affect the reliability and reproducibility of the obtained data. For instance, *in situ* trench logging is very subjective, time-intensive and requires substantial experience, particularly if lighting conditions are unfavourable or deformation features are subtle (Hatheway and Leighton, 1979; McCalpin, 2009). Furthermore, photomosaic logging is usually based on manual rectification and stitching of photographs, which introduces geometric distortions that may lead to misinterpretation. Last but not least, as excavated trenches are usually closed once the outcrop is documented, they remain inaccessible for further analysis or validation, such that the only records of the outcrops preserved are sketches and photo-logs.

With the rise of structure-from-motion (SfM) multiview stereo (MVS) photogrammetric algorithms and advancements in computer vision technology, it has become convenient to produce virtual photogrammetric models (Hodgetts et al., 2004; Buckley et al., 2010; Reitman et al., 2015; Eltner et al., 2016) and orthorectified images that can be used to support palaeoseismic trenching campaigns (Bemis et al., 2014). Ground-based hyperspectral imaging represents an additional technique that has become increasingly popular as a tool in the lithologic characterisation of vertical outcrops (Kurz et al., 2012; Kirsch et al., 2018; Lorenz et al., 2018). Each pixel in hyperspectral imagery (HSI) contains a material-specific spectrum over a certain wavelength range, which can be used to remotely assess compositional variations in geological outcrops. A combination of hyperspectral data cubes and SfM models yields integrated 3D surface models that serve as a robust basis for the logging of palaeoseismic trenches. Whereas hyperspectral imaging of cores and samples has been successfully applied in palaeoseismic studies (Ragona et al., 2006), HSI-enhanced 3D outcrop models of entire trench walls have not yet been employed in palaeoseismic trenching campaigns.

As a case study, hyperspectral imaging is applied on two palaeoseismic trenches dug across a post-glacial fault at the Ristonmännikkö site in the northern Finnish part of the Fennoscandian Shield. Here neotectonic deformation, commonly attributed to post-glacial rebound, has produced discrete reverse fault scarps with small offsets within the Archean basement and glacial-cover sediment sequence. Due to differences in the lithology and deformation style between cover and basement, the studied trenches are mineralogically and structurally very diverse. This makes the Ristonmännikkö site an ideal area to develop and test the proposed hyperspectral approach. As the outcrops are easily accessible, they can be extensively sampled to provide a wealth of validation data. The cold and wet climate of Northern Lapland in September is a challenge for hyperspectral imaging, but this study demonstrates that even hyperspectral data acquired under non-ideal conditions contains distinctive material information to add value to any palaeoseismic campaign.

Geological Setting

The Ristonmännikkö site is located about 30 km south-west of Sodankylä in northern Finnish Lapland. Geologically, the study area is situated within Archean biotite paragneiss overlain by glacial sediments (Fig. 1(a)). Both basement and glacial cover in this area are

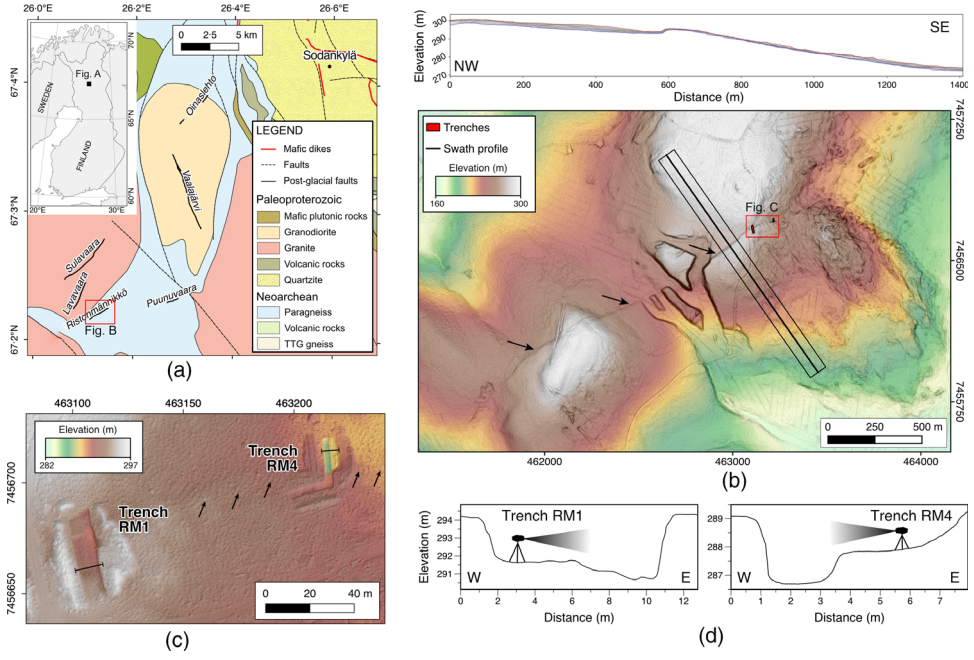

FIG. 1. Overview maps of the study area. (a) Post-glacial faults in northern Lapland (from the paleoseismic database of the Geological Survey of Finland; Palmu et al., 2015). Base maps: 1:1 000 000 geological map from the Geological Survey of Finland. (b) The Ristonmännikkö post-glacial fault and topographic swath profile (100 m width with 5× vertical exaggeration) across the fault scarp (marked by arrows in (b) and (c)) visible in the 2 m lidar DEM from the National Land Survey of Finland. (c) Studied trenches in the north-east part of the Ristonmännikkö post-glacial fault (5 cm DEM generated by UAV photogrammetry). (d) Profiles across trenches RM1 and RM4 showing imaging set-up.

cut by a number of fault segments, the scarps of which are clearly visible in high-resolution digital elevation models (DEMs) as continuous topographic expressions (Fig. 1(b); Ojala et al., 2019). The formation of these faults and their reactivation at various times during different glacial–interglacial cycles is explained by post-glacial isostatic readjustment of the crust (Sutinen et al., 2007, 2014). Other evidence for regional neotectonic activity includes recent seismicity (Ahjos and Uski, 1992; Lagerbäck and Sundh, 2008) and an abundance of potentially earthquake-induced landslides (Ojala et al., 2017, 2018). The Ristonmännikkö (RM) post-glacial fault belongs to the Vaalajärvi post-glacial fault complex (Fig. 1(a)). The associated ENE-trending scarp of the RM post-glacial fault is about 1·8 km long and interpreted to be produced by a low-angle, SE-dipping reverse fault (Ojala et al., 2019).

Two trenches (RM1 and RM4), oriented perpendicular to the Ristonmännikkö fault scarp (Fig. 1(c)), were dug with an excavator and then finely cleaned using a shovel and spatula to best expose mappable stratigraphic and structural contacts. RM1 had a length of about 28 m and a depth of 3·5 m; RM4 had a length of about 14 m and a depth of 2·4 m (Fig. 1(c) and (d)). In these trenches, geological fieldwork revealed a similar stratigraphic and structural architecture (Fig. 2; Ojala et al., 2019): the lower part is composed of highly weathered basement units, namely mica gneiss and migmatitic gneiss intruded by granodiorite and granite, whereas the upper part is made up of two to three differently coloured till units. The two upper till units each have a thickness of about 1 m in both outcrops, whereas the lowermost till is merely half as thick and only present in RM4. The

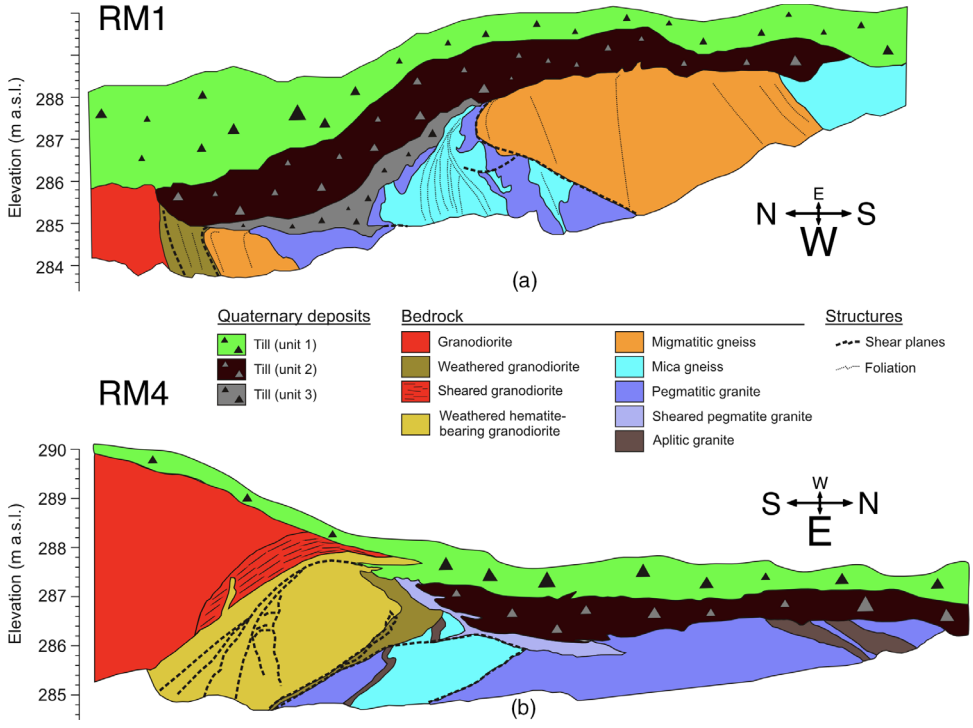

FIG. 2. Geological field sketches of trenches at the Ristonmännikkö (RM) site. Modified after Ojala et al. (2019).

basement is cut by a number of south-dipping low-angle thrust faults (Ojala et al., 2019), the activity of which caused imbrication and thickening of the basement at the location of the scarp, that is in the southern part of the outcrop. Clay-rich fault gouge layers of up to 10 cm thickness can be found along major fault planes. Evidence in RM1 of shearing and drag folding, at the contact between till units 2 and 3 and the basement, indicates that faulting is post-depositional with respect to these two till units. In RM4, basement units form injection lobes into both till units 2 and 1, suggesting the latest increment of fault activation post-dates deposition of both tills (Ojala et al., 2019).

Methods

Photogrammetry

Both terrestrial and unmanned aerial vehicle (UAV) images were employed. The geometry of the trenches was reconstructed using terrestrial images alone in the case of RM4, and with both UAV-based and terrestrial images in the case of RM1. This was done in order to evaluate effort versus benefit of these different approaches. Terrestrial images

Fig. 3. Field logistics involving: (a) excavation of the trench; (b) ground-based hyperspectral imaging using an Aisa FENIX VNIR–SWIR camera; (c) UAV-based photogrammetric survey of the trenches; and (d) field validation (sampling and measurements) using handheld analytical devices (a portable VNIR–SWIR spectrometer is shown).

were captured along two lines at distances of about 5 and 10 m for RM1, and at 4 and 8 m for RM4. These lines were parallel to the wall surface using a Nikon D810 camera (sensor size of 35·9 mm × 24·0 mm, with a pixel count of 7360 × 4912) and a Zeiss Milvus 2/35 ZF.2 lens. The UAV was operated in manual mode, acquiring images with a Nikon Coolpix A camera (sensor size of 23·6 mm × 15·7 mm, with a pixel count of 4928 × 3264) equipped with a Nikon Nikkor 18·5 mm 1:2·8 lens. The camera was mounted on a gimbal with a pitch angle of between about 45° and 80° (increasing pitch with UAV height), programmed to take an image every three seconds. The UAV was manually flown in four lines along the trench axis at heights of 10, 15, 20 to 25 and 30 m above the ground.

Both horizontal and vertical ground control points (GCPs) were deployed prior to image capture (for example, the targets in Fig. 3(c)) to accurately georeference both the photogrammetric and hyperspectral data. A temporary, local reference network was established using a differential Global Navigation Satellite System (GNSS) (Trimble R5 as base and Trimble R4-2 as rover) and later used for locating and orienting the total station (Trimble M3). Observation time per measurement on the rover was set to 10 s. The base station was set up to operate for more than four hours at one fixed position, so its location and height could be calculated with sufficient precision. Each total station measurement was the average of three consecutive measurements of the horizontal and vertical angles and the laser distance. Baseline correction and network optimisation was computed by post-processing using Trimble Business Center software. In addition, permanent GNSS stations from the EUREF network were incorporated in the baseline processing to improve the precision of the base station position.

The 3D outcrop geometry was reconstructed using SfM-MVS photogrammetry as implemented in Agisoft PhotoScan (version 1.2.5) following the protocols outlined by Carrivick et al. (2016) and James et al. (2017a, 2017b, 2019). Processing parameters for the image alignment were set to "high quality" and "reference preselection" was used. Outlier tie points (those detected in fewer than three images or with high residual errors) were subsequently removed using the "gradual selection" tool prior to dense image matching. The threshold for image reprojection errors was set to 0·505 pixels for RM1 and 0·331 pixels for RM4. Images with high residual tie-point errors were excluded from further dense cloud matching. Camera interior and exterior orientation parameters were estimated based on a bundle block adjustment. The dense image matching (or point cloud construction) was run at "high quality" with the depth filtering set to "aggressive".

From each of the photogrammetric models, view-specific (thus corresponding to the position and look direction of the hyperspectral camera) pseudo-orthophotos were generated. These pseudo-orthophotos were co-registered to the HSI using 39 and 88 tie points for RM1 and RM4, respectively, using a thin-plate spline transformation. Registering the orthophoto to the HSI, as opposed to vice versa, eliminates the need for resampling the HSI, which is known to cause degradation of spectral signatures.

Field Validation Data

Validation data was acquired at 37 points on each of the trench walls, including lithological descriptions and analytical data from handheld X-ray fluorescence (XRF) and spectrometer devices (Fig. 3(d)). Additionally, 28 and 35 physical samples were taken for laboratory X-ray diffraction (XRD) analysis for RM1 and RM4, respectively. The coordinates of the sample points of RM1 were measured with a total station using the approach described above. For trench RM4, due to an instrument malfunction, sample

coordinates were extracted from the point cloud by visual comparison with photographs containing the marked sample locations.

Handheld XRF. A portable XRF Bruker S1 Titan 800 (Rh anode; Bruker Corporation, Billerica, USA) was operated to measure the chemical composition of the rock surface at each sampling spot. Prior to measurement, a calibration was conducted with an internal check sample provided by the manufacturer. The data was acquired using the device's GeoChem General settings with 60 s scan time (30 s for elements >Fe; 30 s for elements Fe).

XRD Analysis. Samples were analysed with a Bruker D8 A25 diffractometer (Cu anode). The wavelengths used were Kα_1 = 1·5406, Kα_2 = 1·54439 (Kα_mean = 1·5418), K_β = 1·39222. Adjustments of the generator were 40 kV/40 mA. Randomly orientated samples were prepared by fastening finely ground powder onto a glass plate with acetone. The sample holder was placed into a diffractometer and a spinner was used to improve statistics. Each sample was measured over the range 2 to 70°2Θ, step size 0·02° and measurement time 0·2 s. Phases were identified with Bruker's EVA 4.0 software using the International Centre for Diffraction Data (ICDD) database PDF-4 Minerals 2016. The analysis is semiquantitative and has an accuracy of ±5%.

Handheld Spectrometer Data. A portable Spectral Evolution PSR 3500 spectroradiometer (Spectral Evolution, Lawrence, USA) was used to acquire *in situ* validation spectra. The spectrometer records 1024 bands between 350 and 2500 nm at a spectral resolution of 3·5 nm (1·5 nm sampling distance between 350 and 1000 nm) and 7 nm (2·5 nm sampling distance between 970 and 2500 nm). A contact probe with an artificial light source, focused to an 8 mm wide spot through an optical fibre system, was used in the field to record spectra at all sample spots along the trench wall. For each scan, the mean of 10 consecutive measurements was recorded. Three spots were measured over a 2 cm × 2 cm area at each sample location to even out any lithological heterogeneities. Calibration and conversion from radiance to reflectance was achieved by normalisation with a white polytetrafluoroethylene (PTFE) reference target with a reflectance of >99% in the visible and near-infrared (VNIR) spectrum and >95% in short-wave infrared (SWIR) wavelengths.

Processing of Validation Data. For each set of three reflectance spectra, a centre spectrum was selected to represent a sample location based on a calculation of the minimum Manhattan distance. The centre spectrum constitutes the "physical" sample spectrum closest to the mean, and is therefore considered representative. From these centre spectra, a number of different band ratios were calculated; and from continuum-removed centre spectra, absorption depths were calculated. These allow the evaluation of the relative abundance of selected minerals or chemical groups that produce characteristic absorptions in the VNIR–SWIR spectral range (Hunt, 1977). The identification of depth and the abundance of these chemical groups allows for the evaluation of present lithotypes, their specific supergene alteration and water content.

A band ratio of 750/870 nm calculated on reflectance spectra evaluates the content of ferric oxide minerals, specifically the hematite–goethite ratio, as hematite typically has a reflectance maximum near 750 nm and a minimum between 860 and 880 nm, whereas the extrema for goethite are shifted towards higher wavelengths (Crowley et al., 2003;

Ramanaidou et al., 2015). The presence of the Fe–OH bond characteristic of hydrous silicates, such as chlorites, biotites and amphiboles, was investigated through depth of the absorption at 2243 nm in continuum-removed spectra. The abundance of Al-rich phyllosilicates is analysed based on the depth of the AlOH absorption at 2206 nm; the depth of a feature at 1785 nm is indicative of OH– bonds in smectite group minerals such as montmorillonite and nontronite. The abundance of free water is evaluated based on the depth of the H_2O absorption feature at 1926 nm in continuum-removed spectra. The abundance of the hydroxyl group is analysed based on the depth of absorptions at 1413 nm in the continuum-removed spectrum.

For the statistical evaluation, the analytical validation data was grouped into eight lithological classes based on generalised observations made at the sample locations (Table S1 - see Supplementary Material). RM1 and RM4 samples are considered together, because the respective outcrops are only 100 m apart and exhibit similar lithological and structural characteristics. To visualise the distribution of observations in the multivariate sample space, it is useful to generate biplots (Gabriel, 1971; Greenacre, 2010) based on a principal components analysis (PCA). PCA helps to reduce the dimensions of the dataset by employing an orthogonal projection of the data into a new coordinate system with a minimum loss of information. For a 2D-visualisation, the first two PCA components, PC1 and PC2, are used as the x and y axes of the biplot, in which the projected observation values are represented as points and the projected variables as vectors. Thus, the biplot shows the relationship between input observation values and input variables; the angle between the vectors approximates the correlation between the variables. This helps to evaluate correlations between variables and identify low-variance sub-compositions in the data.

Whereas the sample spectra are visualised in simple PCA biplots, a centred log-ratio (clr) transformation (Aitchison, 1986; Aitchison and Greenacre, 2002) is applied to XRF and XRD compositional data prior to PCA. In biplots based on clr-transformed data the links between apexes represent the log-ratios between two variables. The length of a link is proportional to the variance of the log-ratios of the two variables involved. Two orthogonal links indicate uncorrelated data, whereas parallel links indicate a good correlation.

Hyperspectral Imaging

Data Acquisition. Ground-based hyperspectral data was acquired in cold (about 5 to 10°C), wet (up to 100% relative humidity) and cloudy conditions using a tripod-mounted Aisa FENIX (Specim, Oulu, Finland) hyperspectral pushbroom scanner. The scanner has a vertical field of view of 32·3° (384 pixels) and a maximum horizontal scanning angle of 130°. The camera features a wavelength range of 380 to 2500 nm at a spectral resolution of 3·5 nm in the VNIR and 12 nm in the SWIR. In this study, the sensor was operated using a spectral-binning model (4/1 for the VNIR/SWIR, respectively), resulting in 450 bands. For calibration purposes, a white PTFE reference panel (>99% reflectance in VNIR and >95% in SWIR) was placed in the scene in a similar orientation as the outcrop.

Image Preprocessing. Preprocessing of the hyperspectral image cube follows the workflow described in Jakob et al. (2017), Lorenz et al. (2018) and Kirsch et al. (2018). This includes conversion to at-sensor radiance, lens correction and empirical line correction, followed by co-registration to a photometrically derived, view-specific pseudo-orthophoto and topographic corrections. Topographic correction was achieved using the c-factor approach (Teillet et al., 1982) based on pixel-specific sun incidence angles calculated for

each point of the photogrammetric point cloud and transferred to each pixel of a co-registered pseudo-orthophoto. Further processing of the HSI included masking of the image to remove panels, sky and vegetation, and denoising based on a minimum noise fraction (MNF) transformation (Green et al., 1988). A large part of this procedure is automated in the open-source, Python-based MEPHySTo toolbox (Jakob et al., 2017; Lorenz et al., 2018).

Visualisation. The fully corrected, masked and denoised hyperspectral data cubes were subsequently processed using established image processing algorithms with the purpose of reducing the dimensionality of the HSI so they can be visualised as high-contrast false-colour red/green/blue (RGB) composite images. These HSI-derived RGB false-colour images are then fused with SfM point clouds to produce 25D HSI-enhanced point clouds. The chosen image processing algorithms include both unsupervised feature extraction methods, such as MNF or orthogonal total variation component analysis (OTVCA; Rasti et al., 2016), and mineral mapping methods including minimum wavelength analysis (MWL; van der Meer et al., 2018) and band ratios. MNF and OTVCA were applied on non-denoised images. Whereas MNF uses a linear transformation to reduce noise in selected output channel images (Green et al., 1988), OTVCA uses a total variation (TV) regularisation to extract local neighbourhood information by considering the spatial dependency of adjacent pixels. MNF, MWL and band ratios were generated using the Hyperspectral Python toolbox (HypPy; Bakker et al., 2014) and in-house Python scripts. The OTVCA was performed using a MATLAB script (Rasti et al., 2016), choosing an output number of 20 and 10 features for RM1 and RM4, respectively.

Classification. The classification is based on features extracted by OTVCA that are fed into a support-vector machine (SVM) classifier. Based on the studies reported in Ghamisi et al. (2017), OTVCA outperforms several well-known supervised and unsupervised feature extraction approaches in terms of classification accuracy indices due to its unique capability in extracting spatial information and preserving edges and structures. The training data for the supervised classification is based on image spectra at 30 (RM1) and 33 (RM4) sample locations, labelled according to generalised lithologic descriptions (Table S1). In order to increase the number of training pixels per class and to compensate for any georeferencing, registration and sample-localisation errors, 24 pixels surrounding each of the original training pixels were also included in the training dataset.

Classification was performed using support-vector machine with radial basis function kernel (SVM-RBF, using LibSVM by Chang and Lin, 2011). The algorithm is considered robust even with a low number of training samples as well as potential class heterogeneity, which makes it suitable for the current study. Optimal values for the SVM required parameters C and gamma were traced between 2^{-3} and 2^{4} for gamma and 10^{-2} and 10^{4} for C using five-fold cross validation. Due to the low number of training samples, the assessment of the overall accuracy is based on a qualitative comparison with field sketches rather than traditional numerical metrics.

Extraction of Discontinuities. Discontinuities that may correspond to lithologic boundaries, foliation planes or faults were semi-automatically delineated on various HSI-enhanced point clouds in CloudCompare (version 2.11.alpha) using the CC-Compass plugin (Thiele et al., 2017), which finds the least-cost path between two manually selected points based on RGB similarity and RGB gradient. Geological boundaries, faults and internal contacts were

manually retraced on the RGB point cloud in CloudCompare for comparison. Extracted discontinuities were brought into the open-source desktop geographical information system QGIS (version 3.6) through projective transformation for further editing and presentation.

RESULTS

Photogrammetry

The use of both UAV and ground-based images in the RM1 photogrammetric model, when compared to RM4 where only terrestrial photographs were used, resulted in a denser SfM model with fewer data gaps. However, the RM1 model also exhibited slightly higher reprojection and GCP errors than RM4 (Table I), possibly due to the lower resolution of the UAV camera. Relative to a sub-vertical plane fitted through the points composing the steep

TABLE I. Reconstruction parameters of the SfM models. RM1 uses both terrestrial and UAV images; RM4 uses only terrestrial images.

SfM model	*No. of images*	*No. of GCPs*	*Reprojection error (pixel)*	*GCP error (total in cm)*	*GCP error in X, Y, Z (cm)*
RM1	213	23	0·505	2·68	0·79, 0·83, 2·43
RM4	89	13	0·331	0·315	0·224, 0·197, 0·103

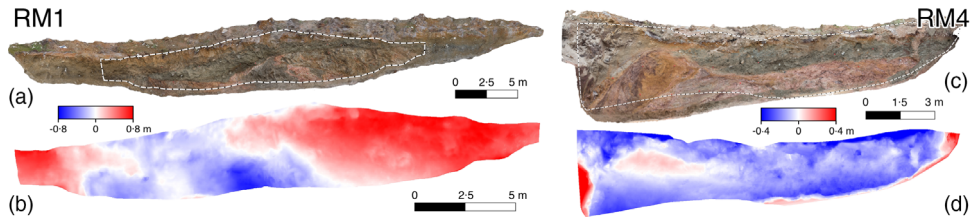

FIG. 4. RM1 and RM4 trench walls. (a), (c) SfM photogrammetry-derived pseudo-orthophotos of the studied trench walls. Stippled lines delineate the areal extent of the respective hyperspectral scan after masking. (b), (d) Elevation relative to mean sub-vertical projection plane.

section of the outcrop, the trench walls displayed a relief of 1·6 and 0·8 m for RM1 and RM4, respectively (Fig. 4(b) and (d)). As a result, projection of these point clouds to obtain traditional 2D photo-logs led to distortions, so geologic analyses of these outcrops are best performed based on the actual point clouds within a 3D environment.

Hyperspectral Imaging

Hyperspectral scanning and preprocessing yielded two fully calibrated and corrected hyperspectral data cubes covering nearly the entire trench walls of RM1 and RM4 (Figs. 4(a) and (c)) with a ground resolution of between 1 and 3 cm. Contrast-enhancing pseudo-coloured images of MNF, OTVCA, band ratios and MWL highlight stratigraphic and structural features of the basement and cover sequence exposed in the trench outcrops (Fig. 5). Given the partial automation of the image pre- and post-processing procedures, these images can be prepared within a few hours (a few minutes considering pure processing time) to assist the geologist on site. When merged with SfM photogrammetric models, the

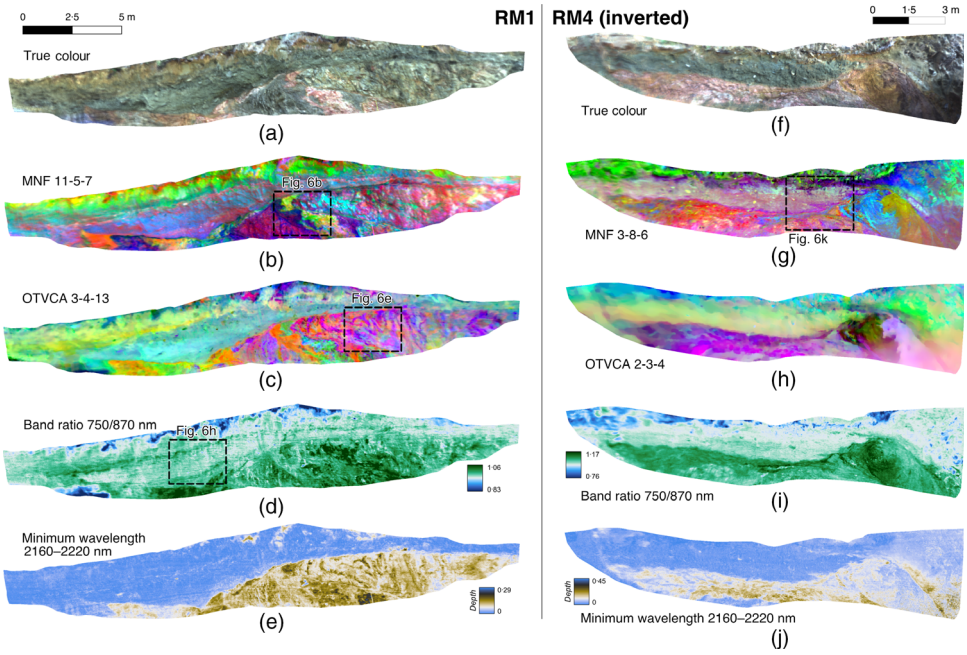

FIG. 5. Contrast-enhancing hyperspectral imaging products (orthographic projection). MNF = minimum noise fraction; OTVCA = orthogonal total variation component analysis.

images yield undistorted, HSI-enhanced point clouds that can serve as a basis for the delineation of lithological contacts and shear planes in a 3D environment. (See https://www.hzdr.de/FWG/FWGE/Hyperclouds/Hypertrenches.html for an interactive visualisation of a selection of the presented HSI-enhanced point clouds in the web-based Potree viewer. Individual point clouds are available as supplementary data at https://doi.pangaea.de/10.1594/PANGAEA.904718.)

The MNF and OTVCA images highlight the lithological heterogeneity and internal structures of the basement, such as the irregular intrusive contact between mica gneiss and pegmatite granite in RM1 (Figs. 5(b) and 6(a) to 6(c)) and fold-like structures within migmatitic gneiss in RM1 (Figs. 5(c) and 6(d) to 6(f)). Band ratio and MWL images emphasise the compositional differences between basement and cover (Fig. 5(d), (e), (i) and (j)), indicating a comparatively higher abundance of Fe^{3+}- and AlOH-bearing minerals in the basement. In RM1, particularly high iron abundances are identified within the main migmatitic gneiss unit and in the pegmatite granite near the bottom apex with till unit 3. Within the cover of RM1, linear features of higher iron indices coincide with mapped tops of distinct till units (Figs. 5(d) and 6(g) to 6(i)). Moreover, various HSI images locally show thin, distinctly coloured layers at unit interfaces (Fig. 5(b) and (g)), most of which correspond to mapped shear planes (Fig. 2). In addition to the mapped shear planes, a thin layer occurs at the base of tills 2 and 3 in the northern part of RM1, suggesting that the nature of this contact is tectonic. In places, lithologic units are offset along these layers, for example fragments of pegmatite granite near the bottom apex of till 3 in RM1 (Figs. 5(b) and (e)) and multiple blocks of different lithologies north of a weathered hematite-bearing

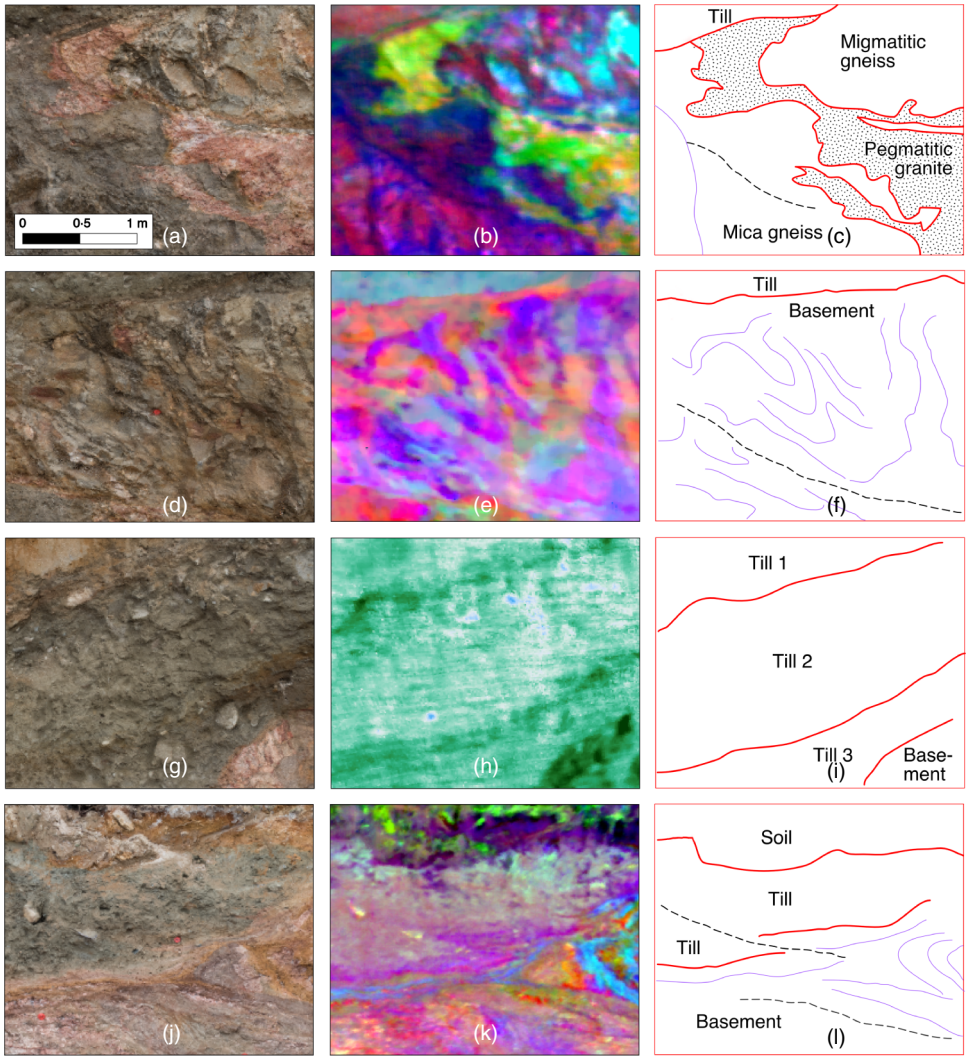

FIG. 6. Close-ups of stratigraphic/structural features that are particularly conspicuous in the hyperspectral images. Left column: RGB images. Centre column: HSI products. Right column: geologic interpretation (red = lithological boundary; blue = internal contact; stippled black = inferred fault). First row (a–c): irregular, lobate intrusive contact between mica gneiss and pegmatite granite. Second row (d–f): ductile structures in the basement units of RM1 (OTVCA 3-4-13). Third row (g–i): supergene alteration marking the tops of main lithologic units of RM1 (BR 750/870 nm). Fourth row (j–l): fault in RM4, displacing both basement and cover units (MNF 3-8-6).

granodiorite unit in the centre part of RM4 (Fig. 5(g) to (i)). At least one of these anisotropies appears to be continuous into till 2 of RM4 (Figs. 5(f) and 6(j) to 6(l)).

The classification maps obtained with the supervised classifier that is based on labelled image samples are generally in very good agreement with the field sketches (Fig. 7). In RM1, discrepancies between the classifications and the field sketches include: (i) a more

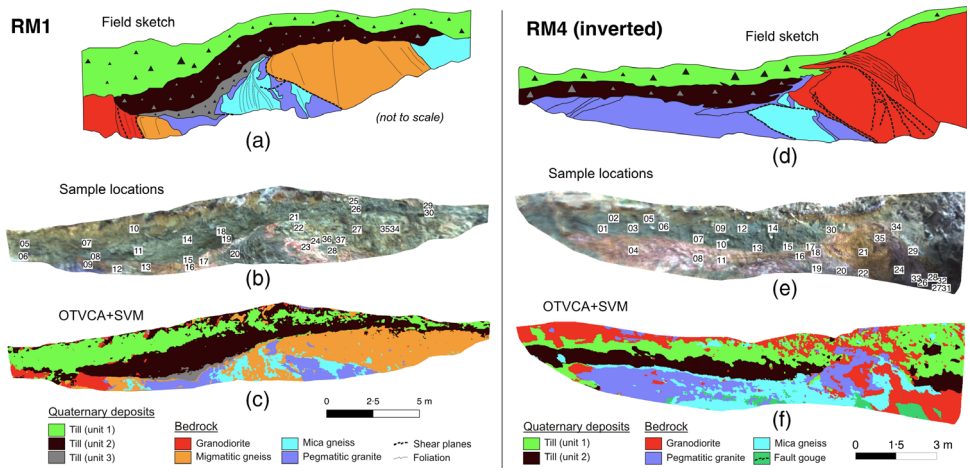

FIG. 7. Supervised classifications based on lithological descriptions at marked sample locations in (b) and (f). Generalised field sketches modified after Ojala et al. (2019). Abbreviations: OTVCA = orthogonal total variation component analysis; SVM = support-vector machines.

jagged contact between till units 1 and 2; (ii) an additional occurrence of migmatitic gneiss within the mica gneiss unit in the centre of the outcrop; and (iii) a missing unit mapped as mica gneiss in the right side of the field sketch. In RM4, there are some apparent misclassifications of granodiorite in the upper till unit and a very diffuse boundary between the pegmatite granite and the mica gneiss in the basement.

A total of 87 discontinuities for RM1 and 38 discontinuities for RM4 were semi-automatically extracted based on visual inspection of a variety of HSI-enhanced point clouds of the respective trench outcrops. The serrated shape of these discontinuities is a

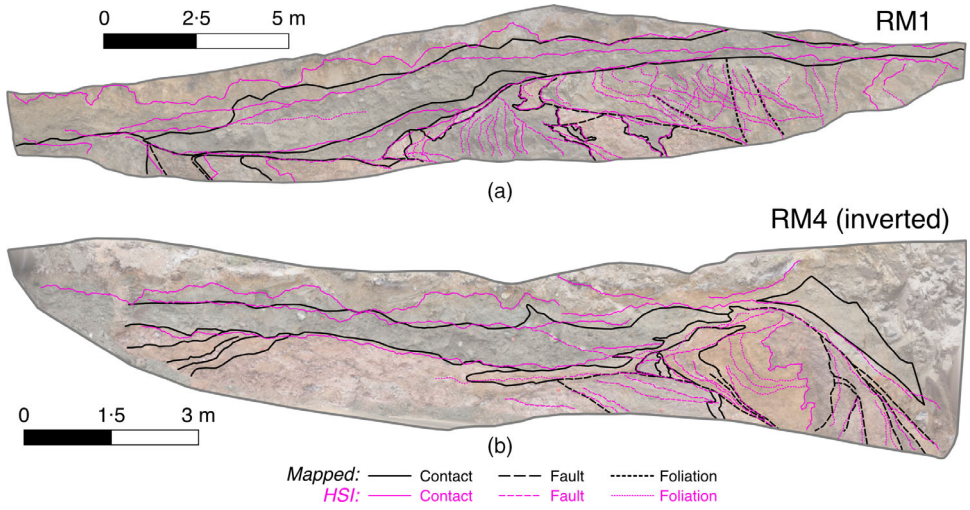

FIG. 8. Discontinuities extracted manually from the RGB point clouds and semi-automatically from various HSI-enhanced 3D point clouds.

combined effect of point cloud topography and the orthographic projection of the discontinuities. A comparison of mapped and HSI-derived discontinuities (Fig. 8) in general shows good correlation. All major lithologic boundaries, faults and foliations mapped in the field could also be identified in HSI-enhanced point clouds. There are some discrepancies in the mapped versus extracted limits between: (i) the pegmatite granite and migmatitic gneiss unit in the northern part of RM1 (~50 cm offset); (ii) till units 2 and 1 both in RM1 and RM4; (iii) aplite granite and host rock in RM4 (not apparent in HSI); and (iv) sheared and unsheared granodiorite in RM4 (not apparent in HSI). In terms of structures, all but two small shear planes mapped in RM1 (a sub-horizontal shear in the pegmatite granite and a folded shear plane in the weathered granodiorite) could be delineated in the HSI-enhanced point clouds. The HSI point clouds locally contain more detail than their RGB counterparts, yielding discontinuities that find no equivalent in the field sketches (Fig. 2) and could arguably be interpreted as either lithologic contacts, internal contacts or faults (Fig. 8).

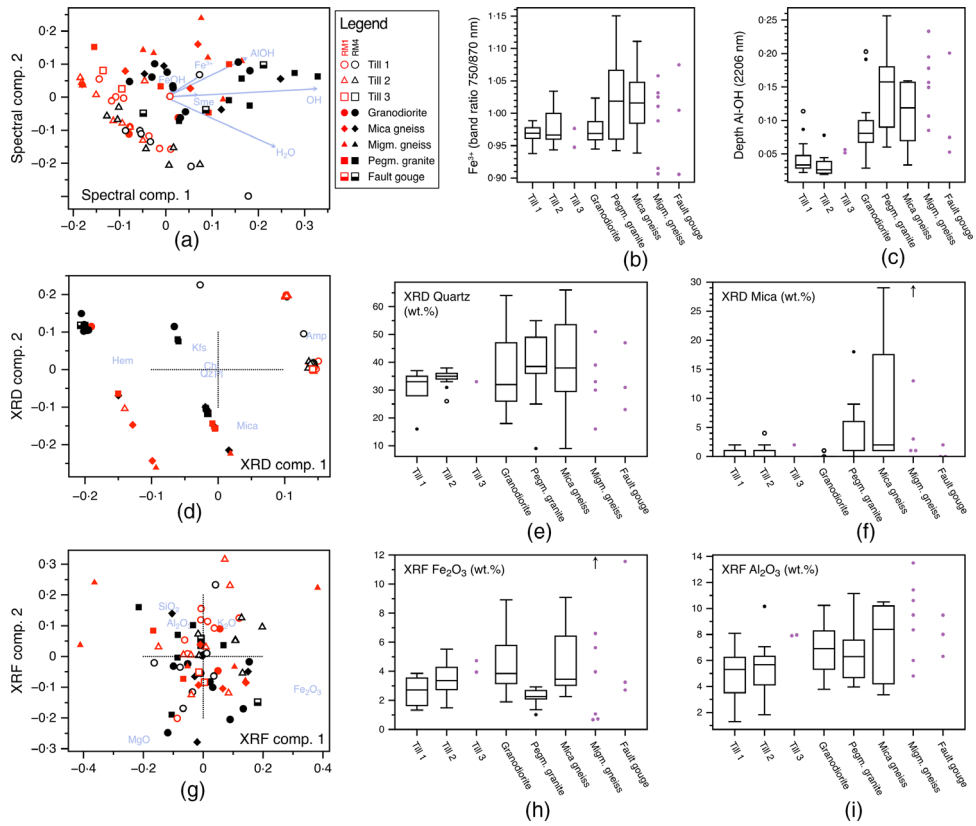

FIG. 9. Multivariate statistics of analytical validation data. Top row (a–c): spectrometer data. Middle row (d–f): X-ray diffraction data. Bottom row (g–i): X-ray fluorescence data. (a), (d) and (g) are compositional principal component analysis (PCA) biplots (see text for details); for (d) and (g), a centred log-ratio transformation was applied to the data prior to PCA. Boxplots are only drawn if n 8, otherwise purple jitter points are used. Outliers marked by filled and unfilled black circles. One outlier is omitted from (a) for clarity (migmatitiv gneiss RM1-37 at x, $y = -0{\cdot}16$, $0{\cdot}49$). Mineral abbreviations after Whitney and Evans (2010).

Validation Data

Spectral indices calculated from spectrometer data indicate that there is a clear compositional contrast between basement and cover units, with the basement exhibiting deeper absorptions associated with AlOH- and Fe^{3+}-bearing phases as well as smectite group minerals (Fig. 9(a)–(c)). This observation agrees with Fe^{3+} band ratio images and AlOH minimum wavelength maps (Fig. 9(d), (e), (h) and (i)). The intra-formational spectral variance, particularly regarding the till, can be explained by differences in the water content (porosity). The relatively higher abundance of AlOH- and Fe-bearing minerals in the basement is supported by higher mica and hematite content in some of the basement units (XRD data; Fig. 9(d) and (e)), and slightly elevated Fe_2O_3 and Al_2O_3 values in basement lithologies relative to till (XRF data; Fig. 9(g)–(i)). XRD analysis, furthermore, reveals that the till, while comparably depleted in hematite and mica, shows similar abundance in quartz, plagioclase and chlorite, but is relatively enriched in amphibole.

Image spectra from the eight lithological classes of the trenches (Fig. 10) show very

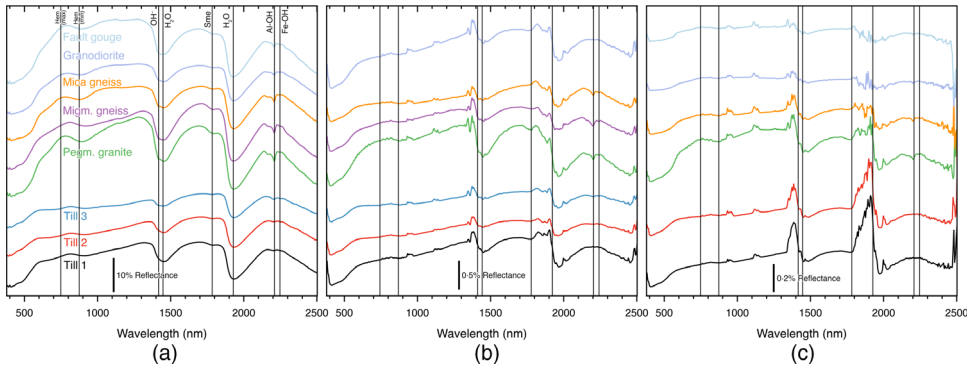

FIG. 10. Representative VNIR–SWIR spectra of lithologies in the two studied trenches. (a) *In situ* spectrometer data from both trenches. (b) RM1 and (c) RM4 image spectra extracted from the hyperspectral image. Spectra vertically offset for clarity.

good agreement to the spectrometer data regarding diagnostic absorption features (such as Fe^{3+}, AlOH and smectite features) despite lower reflectance values, especially for trench RM4. Another important observation to be made in this spectral comparison is the high noise in the SWIR part of the image spectra at wavelengths above 2300 nm and a high influence on water absorption in the spectra, suggesting high air moisture and/or water covering the surface of the outcrop.

DISCUSSION

Accuracy and Biases

The radiometric quality of the hyperspectral scans strongly depends on weather conditions during data acquisition. In the present case study, damp, cold and cloudy conditions had a clear negative effect on the signal-to-noise level of the hyperspectral data (more so on RM4 than RM1), which is manifested by low reflectance values (Fig. 10(b) and (c)), strong water absorption in the spectra and noisy image and classification results.

However, the case study shows that diagnostic absorption features are still recognisable in the image spectra despite these unfavourable conditions, so hyperspectral imaging can yield useful information and add value to any palaeoseismic campaign.

The geometric accuracy of the final HSI-enhanced virtual models is a function of the following three factors:

(1) *The quality of the SfM models*. In the present case study, this was validated and iteratively improved based on the measured GCP positions and estimated GCP positions using the Monte-Carlo approach presented by James et al. (2017b). Based on the results of this simulation, one GCP for trench RM1 was discarded due to a high error. The average error of the GCPs in RM1 is 2·68 cm and in RM4 is 0·315 cm (Table I).
(2) *The positioning of the hyperspectral instrument relative to the outcrop*. A noticeable difference in sharpness of the HSI of RM4 from the southern to northern side of the outcrop reflects the decision to place the scanner opposite of the southern part of the outcrop that exposes the fault scarp. Due to the limited distance between the scanner and the trench wall (RM1: about 8·5 m; RM4: about 5 m), and the panoramic image acquisition of a wide (RM1: about 25 m; RM4: about 15 m) nearly planar outcrop, this resulted in a very oblique scanning angle (about 60°) for the northern part of the outcrop. Hence, whereas the ground resolution of the hyperspectral scans is about 1 cm in the part of the outcrop closest to the scanner, it decreases to about 3 cm towards the edges.
(3) *The error of the co-registration between pseudo-orthophoto and hyperspectral image*. In this case study, a total number of 39 and 88 tie points were used for the co-registration of RM1 and RM4, respectively. The co-registration accuracy was evaluated using 12 handpicked control points for each of the hyperspectral images (see Salehi et al., 2018, for details on the procedure), resulting in a root mean square error (RMSE) in X, Y, Z of 1·6/2·1/4·3 cm for RM1 and 0·6/2·5/3·2 cm for RM4.

The geometric errors listed above are small compared to the size of the identified geological features and are thus not expected to affect trench interpretation. As a recommendation regarding the positioning of the hyperspectral scanner to minimise distortions and loss of resolution towards the right and left edges of the scan, the scanning angle should not exceed 45°, in other words the ratio of the target-to-sensor distance to the target width should ideally be above 0·5 for planar outcrops. For wider targets, it is recommended to scan from multiple positions along the target.

Discrepancies between the field-mapped lithological information and the classification image may be caused by any, or a combination, of the following factors:

(1) Differences between certain lithologies based on minerals not active in the SWIR (for example, migmatitic versus mica gneiss).
(2) Great heterogeneity within one lithological unit.
(3) Actual draping of lithologies (such as till covering granodiorite in RM4).
(4) Soil processes and downward penetration of soil water, which may have caused chemical weathering of different lithologies.
(5) Distortions of the field sketch relative to the orthogonally projected classification image.
(6) Misinterpretation during geological mapping.

Another source for potential mismatches between lithological logs and classification for RM1 comes from the fact that a partial collapse (approximately $3\,m \times 3\,m$) occurred in the centre of the trench wall during the time between the measurement of sample coordinates and photo acquisition to produce the photogrammetric model. The slump is manifested in higher distances between sample points and the point cloud for certain sample points in the centre of the trench wall, which may have produced a slight shift of lithological boundaries. This, in turn, may have caused training pixels to fall on lithological edges or within a different domain altogether. However, as the sample points were mostly placed in the centre of lithological units, the slump is unlikely to have had a profound influence on the classification results.

Disagreements between discontinuities mapped in the field and those extracted from HSI-enhanced point clouds may be due to: (i) the manual/semi-automatic method of discontinuity extraction; (ii) low textural/compositional contrast between two units; (iii) the oblique scanning angle, particularly relative to the northern part of RM4; (iv) diffuseness of compositional (chemical) boundaries; or (v) draping of outcropping lithologies by loose material from above.

Like any analysis that involves human interaction, the described workflow is affected by certain biases, starting with image acquisition, where the set-up geometry and the choice of frame rate versus integration time versus scanning speed during the scanning process can significantly influence the quality of the raw hyperspectral data cube. The image processing was based on a defined sequence of steps to transform the raw hyperspectral data cubes into meaningful images and virtual models. However, some of the processing steps require manual input, such as: (i) the type of topographic correction method; (ii) the degree of smoothing; (iii) the number of features and TV coefficient for the OTVCA; (iv) the selection of bands for the pseudo-coloured images and the SVM classifications; and (v) the radius around sample pixels to be included as training data for the classification. Despite these biases, the information gained by the described approach can significantly improve the interpretability of palaeoseismic trenching data.

Added Value of the Approach

Hyperspectral imaging can easily be integrated into palaeoseismic trenching campaigns. Although employing heavy equipment, the transportation and set-up of hyperspectral instruments can take advantage of the infrastructure and excavation logistics that usually accompany palaeoseismologic fieldwork. The current hyperspectral sensor development focused on increasing spectral resolution and range while decreasing instrument size and cost (Adão et al., 2017; Ziph-Schatzberg et al., 2018) will further improve the practicability of employing hyperspectral sensors, particularly in remote areas.

In terms of geological interpretation, the study has shown that there are several advantages to using HSI-enhanced virtual outcrop models as a complement to traditional palaeoseismic analyses. These include the following:

(1) *Compositional information*. Such information, based on the material-characteristic spectral reflectance properties, provides objective and interpretable data and a versatile data archive. Based on the analysis of key absorption features in the VNIR–SWIR hyperspectral data (and proper ground validation), colour differences in the HSI can be related to mineralogy. For instance, the colour contrast between basement and cover units in both trenches is clearly related to higher abundances

of white mica/clay and hematite in the basement (Figs. 5(d), (e), (i), (j) and 9(a) to (c)). Phyllosilicates in the basement concentrate along thin features that correspond to foliations, highlighted by folds identified in migmatitic gneiss of RM1, and shear planes, such as those forming the imbricated thrust stack north of the large lensoidal granitoid block in RM4. In RM1, layer-parallel iron enrichment in the till units (Figs. 5(d) and 6(d) to 6(f)) is likely to be related to a surficial enrichment of iron (hydr)oxides as the tills became exposed to supergene weathering after deposition.

(2) *Processed hyperspectral data cubes*. These provide contrast-rich images and classifications that enable the identification of geological units and structures with high accuracy. These hyperspectral products can be made available to the geologist on site within a few hours to assist ongoing fieldwork, for example by using HSI-derived features or classification mismatches to guide or verify field observations. The timing aspect is particularly relevant in trenching campaigns, where the outcrops are only temporary.

(3) *Hidden features*. Hyperspectral imagery can reveal stratigraphic and structural features hidden to the unaided eye. This case study demonstrated that interpretations based on field observations and photo-logs agree well with the interpretations derived from the hyperspectral images and vice versa. However, based on HSI, a number of additional foliation surfaces, folds and shear planes were identified in the Ristonmännikkö trenches that were not directly apparent in the visible part of the spectrum. Amongst these is a shear plane that offsets the uppermost basement unit of RM4 (pink triangle-shaped block in Figs. 5(g) and 6(g) to 6(i), described as an injection lobe by Ojala et al., 2019) and continues into till unit 2 above. The continuation of this structure into the till is significant, because it would prove that the deposition of the till pre-dated the latest increment of regional palaeoseismic activity. This structure, once identified in a preliminarily processed hyperspectral image that was available to the geologist on site, could subsequently be verified in the field. Another HSI-derived potentially crucial observation is the thin layer discernible at the base of tills 2 and 3 in the northern part of RM1 (Fig. 5(b)), suggesting that the nature of this contact is tectonic and may constitute the prolongation of the mapped fault below the migmatitic gneiss/pegmatitic granite unit in the centre of the outcrop.

(4) *HSI–SfM combination*. Any HSI product can be combined with SfM point clouds to produce HSI-enhanced virtual outcrop models, which provide a three-dimensional, distortion-free framework for intuitive outcrop visualisation and analysis. As 3D base maps, these models can be used to delineate and analyse/measure geologic contacts and structures using manual or semi-automatic discontinuity extraction methods. Within the 3D framework, sample-based (spatially referenced) analytical data is easily incorporated during interpretation. HSI-derived discontinuities can be correlated across outcrops and integrated with digital elevation modes, drill-core and geophysical data such as ground-penetrating radar surveys that are often included in palaeoseismic studies (McCalpin, 2009). Textural information is available through high-resolution SfM photogrammetric models from which structural measurements of linear and (if conditions allow) planar elements can be obtained.

Conclusions

This study showcases a workflow to produce a geometrically and radiometrically corrected combination of an SfM point cloud and a VNIR–SWIR hyperspectral data cube of vertical outcrops to be used as support for palaeoseismic trenching campaigns. There are six main outcomes of the presented case study:

(1) HSI-enhanced point clouds provide undistorted, contrast-rich 3D base maps for the delineation of sedimentary and tectonic structures. Extracted discontinuities based on these point clouds confirmed previously field-mapped structures and highlighted additional features that were barely visible to the naked eye. Some of the structures identified in HSI were validated in the field.
(2) Laboratory and *in situ* analytical data proved useful for the validation of the spectral features and provided a link between spectral and mineralogical/chemical composition.
(3) Logistical requirements for the generation of HSI-enhanced virtual outcrop models include a slightly modified trench geometry to allow placement of the tripod-mounted sensor. Despite low absolute reflectance values and noisy image spectra caused by unfavourable weather conditions during acquisition, diagnostic absorption features could still be recognised.
(4) The spatial accuracy of the HSI-enhanced point clouds, which is a function of the quality of the SfM model, the acquisition geometry and the HSI–SfM co-registration error, is calculated to be within a few centimetres. Due to the topography of the outcrop wall, projections of this HSI-enhanced point cloud can lead to distortions, so analyses are best performed within a 3D environment.
(5) Pre- and post-processing of the HSI is accomplished using a partially automated workflow and established image processing routines, which reduces user interaction and associated biases. The presented processing routines use open-source software and are adaptable to datasets from a variety of hyperspectral sensors. The time required for the preparation of HSI-enhanced point clouds is in the range of a few hours, so the models can be available in time to assist geological mapping; they remain available as a versatile data archive even after the trench is closed.
(6) The described approach is suitable for geological mapping of basement rocks and sedimentary deposits alike, which makes it applicable in geological research, mineral resource exploration and the mining industry.

Acknowledgements

Irmeli Huovinen, Aleksi Sutinen and Pasi Heikkilä (GTK) are gratefully acknowledged for conducting, organising and interpreting the XRD analysis. This paper is a part of the cooperation project PGSdyn carried out between Posiva Oy and the Geological Survey of Finland (GTK).

Supporting Information

Additional Supporting Information may be found in the online version of this article:

Table S1. Sample locations and validation data for palaeoseismic trenches RM1 and RM4, Finnish Lapland, including lithological descriptions, portable spectrometer data in the

visible and near-infrared (VNIR) and short-wave infrared (SWIR) range, portable X-ray fluorescence (XRF) data, and X-ray diffraction (XRD) data.

REFERENCES

Adão, T., Hruška, J., Pádua, L., Bessa, J., Peres, E., Morais, R. and Sousa, J. J., 2017. Hyperspectral imaging: a review on UAV-based sensors, data processing and applications for agriculture and forestry. *Remote Sensing*, 9(11): article 1110. 31 pages.

Ahjos, T. and Uski, M., 1992. Earthquakes in northern Europe in 1375–1989. *Tectonophysics*, 207(1–2): 1–23.

Aitchison, J., 1986. *The Statistical Analysis of Compositional Data*. Chapman & Hall, London, UK. 416 pages.

Aitchison, J. and Greenacre, M., 2002. Biplots of compositional data. *Journal of the Royal Statistical Society: Series C (Applied Statistics)*, 51(4): 375–392.

Bakker, W. H., van Ruitenbeek, F. J. A., van der Werff, H. M. A., Zegers, T. E., Oosthoek, J. H. P., Marsh, S. H. and van der Meer, F. D., 2014. Processing OMEGA/Mars Express hyperspectral imagery from radiance-at-sensor to surface reflectance. *Planetary and Space Science*, 90: 1–9.

Bemis, S. P., Micklethwaite, S., Turner, D., James, M. R., Akciz, S., Thiele, S. T. and Bangash, H. A., 2014. Ground-based and UAV-based photogrammetry: a multi-scale, high-resolution mapping tool for structural geology and paleoseismology. *Journal of Structural Geology*, 69(Part A): 163–178.

Buckley, S. J., Enge, H. D., Carlsson, C. and Howell, J. A., 2010. Terrestrial laser scanning for use in virtual outcrop geology. *Photogrammetric Record*, 25(131): 225–239.

Carrivick, J. L., Smith, M. W. and Quincey, D. J., 2016. *Structure from Motion in the Geosciences*. Wiley-Blackwell, Chichester, UK. 208 pages.

Chang, C.-C. and Lin, C.-J., 2011. LIBSVM: a library for support vector machines. *ACM Transactions on Intelligent Systems and Technology*, 2(3): article 27. DOI: https://doi.org/10.1145/1961189.1961199

Crowley, J. K., Williams, D. E., Hammarstrom, J. M., Piatak, N., Chou, I.-M. and Mars, J. C., 2003. Spectral reflectance properties (04–25 μm) of secondary Fe-oxide, Fe-hydroxide, and Fe-sulphate-hydrate minerals associated with sulphide-bearing mine wastes. *Geochemistry: Exploration, Environment, Analysis*, 3(3): 219–228.

Eltner, A., Kaiser, A., Castillo, C., Rock, G., Neugirg, F. and Abellán, A., 2016. Image-based surface reconstruction in geomorphometry – merits, limits and developments. *Earth Surface Dynamics*, 4(2): 359–389.

Gabriel, K. R., 1971. The biplot graphic display of matrices with application to principal component analysis. *Biometrika*, 58(3): 453–467.

Ghamisi, P., Yokoya, N., Li, J., Liao, W., Liu, S., Plaza, J., Rasti, B. and Plaza, A., 2017. Advances in hyperspectral image and signal processing: a comprehensive overview of the state of the art. *IEEE Geoscience and Remote Sensing Magazine*, 5(4): 37–78.

Green, A. A., Berman, M., Switzer, P. and Craig, M. D., 1988. A transformation for ordering multispectral data in terms of image quality with implications for noise removal. *IEEE Transactions on Geoscience and Remote Sensing*, 26(1): 65–74.

Greenacre, M., 2010. *Biplots in Practice*. Fundación BBVA, Bilbao, Spain. 240 pages.

Hatheway, A. W. and Leighton, F. B., 1979. Trenching as an exploratory method. Chapter 12 in Geology in the Siting of Nuclear Power Plants (Eds. A. W. Hatheway and C. R. McClure). *Reviews in Engineering Geology*, Volume IV. Geological Society of America, Boulder, Colorado, USA. 257 pages: 169–196.

Hodgetts, D., Drinkwater, N. J., Hodgson, J., Kavanagh, J., Flint, S. S., Keogh, K. J. and Howell, J. A., 2004. Three-dimensional geological models from outcrop data using digital data collection techniques: an example from the Tanqua Karoo depocentre, South Africa. *Geological Society of London Special Publications*, 239(1): 57–75.

Hunt, G. R., 1977. Spectral signatures of particulate minerals in the visible and near infrared. *Geophysics*, 42(3): 501–513.

Jakob, S., Zimmermann, R. and Gloaguen, R., 2017. The need for accurate geometric and radiometric corrections of drone-borne hyperspectral data for mineral exploration: MEPHySTo – a toolbox for pre-processing drone-borne hyperspectral data. *Remote Sensing*, 9(1): article 88. 17 pages. DOI: https://doi.org/10.3390/rs9010088

James, M. R., Robson, S., d'Oleire-Oltmanns, S. and Niethammer, U., 2017a. Optimising UAV topographic surveys processed with structure-from-motion: ground control quality, quantity and bundle adjustment. *Geomorphology*, 280: 51–66.

James, M. R., Robson, S. and Smith, M. W., 2017b. 3-D uncertainty-based topographic change detection with structure-from-motion photogrammetry: precision maps for ground control and directly georeferenced surveys. *Earth Surface Processes and Landforms*, 42(12): 1769–1788.

James, M. R., Chandler, J. H., Eltner, A., Fraser, C., Miller, P. E., Mills, J. P., Noble, T., Robson, S. and Lane, S. N., 2019. Guidelines on the use of structure-from-motion photogrammetry in geomorphic research. *Earth Surface Processes and Landforms*, 44(10): 2081–2084. DOI: https://doi.org/10.1002/esp.4637

Kirsch, M., Lorenz, S., Zimmermann, R., Tusa, L., Möckel, R., Hödl, P., Booysen, R., Khodadadzadeh, M. and Gloaguen, R., 2018. Integration of terrestrial and drone-borne hyperspectral and photogrammetric sensing methods for exploration mapping and mining monitoring. *Remote Sensing*, 10(9): article 1366. 31 pages.

Kurz, T. H., Buckley, S. J. and Howell, J. A., 2012. Close-range hyperspectral imaging for geological field studies: workflow and methods. *International Journal of Remote Sensing*, 34(5): 1798–1822.

Lacan, P., Ortuño, M., Audin, L., Perea, H., Baize, S., Aguirre-Díaz, G. and Zúñiga, F. R., 2018. Sedimentary evidence of historical and prehistorical earthquakes along the Venta de Bravo Fault System, Acambay Graben (Central Mexico). *Sedimentary Geology*, 365: 62–77.

Lagerbäck, R. and Sundh, M., 2008. *Early holocene faulting and paleoseismicity in Northern Sweden*. Research Paper C 836, Geological Survey of Sweden, Uppsala, Sweden. 80 pages.

Lorenz, S., Salehi, S., Kirsch, M., Zimmermann, R., Unger, G., Vest Sørensen, E. and Gloaguen, R., 2018. Radiometric correction and 3D integration of long-range ground-based hyperspectral imagery for mineral exploration of vertical outcrops. *Remote Sensing*, 10(2): article 176. 23 pages.

McCalpin, J. P., 2009. *Paleoseismology. International Geophysics*, Volume 95. Second edition. Academic Press, Burlington, Massachusetts, USA. 613 pages.

van der Meer, F., Kopačková, V., Koucká, L., van der Werff, H. M. A., van Ruitenbeek, F. J. A. and Bakker, W. H., 2018. Wavelength feature mapping as a proxy to mineral chemistry for investigating geologic systems: an example from the Rodalquilar epithermal system. *International Journal of Applied Earth Observations and Geoinformation*, 64: 237–248.

Ojala, A. E. K., Mattila, J., Markovaara-Koivisto, M., Ruskeeniemi, T., Palmu, J.-P. and Sutinen, R., 2017. Distribution and morphology of landslides in northern Finland: an analysis of postglacial seismic activity. *Geomorphology*, 326: 190–201.

Ojala, A. E. K., Markovaara-Koivisto, M., Middleton, M., Ruskeeniemi, T., Mattila, J. and Sutinen, R., 2018. Dating of paleolandslides in western Finnish Lapland. *Earth Surface Processes and Landforms*, 43(11): 2449–2462.

Ojala, A. E. K., Mattila, J., Ruskeeniemi, T., Markovaara-Koivisto, M., Palmu, J.-P., Nordbäck, N., Lindberg, A., Aaltonen, I., Savunen, J. and Sutinen, R., 2019. *Postglacial Faults in Finland – a Review of PGSdyn Project Results*. Posiva Oy, Eurajoki, Finland. 117 pages.

Palmu, J.-P., Ojala, A. E. K., Ruskeeniemi, T., Sutinen, R. and Mattila, J., 2015. LiDAR DEM detection and classification of postglacial faults and seismically-induced landforms in Finland: a paleoseismic database. *GFF (Journal of the Geological Society of Sweden)*, 137(4): 344–352.

Ragona, D., Minster, B., Rockwell, T. and Jussila, J., 2006. Field imaging spectroscopy: a new methodology to assist the description, interpretation, and archiving of paleoseismological information from faulted exposures. *Journal of Geophysical Research: Solid Earth*, 111(B10): article B10309. 11 pages.

Ramanaidou, E., Wells, M., Lau, I. and Laukamp, C., 2015. Characterization of iron ore by visible and infrared reflectance and Raman spectroscopies. *Chapter 6 in Iron Ore: Mineralogy, Processing and Environmental Sustainability* (Ed. L. Lu). Woodhead, Cambridge, UK. 666 pages: 191–228.

Rasti, B., Ulfarsson, M. O. and Sveinsson, J. R., 2016. Hyperspectral feature extraction using total variation component analysis. *IEEE Transactions on Geoscience and Remote Sensing*, 54(12): 6976–6985.

Reitman, N. G., Bennett, S. E. K., Gold, R. D., Briggs, R. W. and DuRoss, C. B., 2015. High-resolution trench photomosaics from image-based modeling: workflow and error analysis. *Bulletin of the Seismological Society of America*, 105(5): 2354–2366.

Rockwell, T. K. and Ben-Zion, Y., 2007. High localization of primary slip zones in large earthquakes from paleoseismic trenches: observations and implications for earthquake physics. *Journal of Geophysical Research: Solid Earth*, 112(B10): article B10304. 12 pages. DOI: https://doi.org/10.1029/2006JB004764

Salehi, S., Lorenz, S., Vest Sørensen, E., Zimmermann, R., Fensholt, R., Henning Heincke, B., Kirsch, M. and Gloaguen, R., 2018. Integration of vessel-based hyperspectral scanning and 3D-photogrammetry for mobile mapping of steep coastal cliffs in the Arctic. *Remote Sensing*, 10(2): article 175. 26 pages.

Sutinen, R., Piekkari, M. and Liwata, P., 2007. *Time-transgressive evolution of landslides possibly induced by seismotectonic events in Lapland*. Geological Survey of Finland Special Paper 46 (Applied Quaternary Research in the Central Part of Glaciated Terrain): 121–128.

Sutinen, R., Hyvönen, E., Middleton, M. and Ruskeeniemi, T., 2014. Airborne LiDAR detection of postglacial faults and Pulju moraine in Palojärvi, Finnish Lapland. *Global and Planetary Change*, 115: 24–32.
Teillet, P. M., Guindon, B. and Goodenough, D. G., 1982. On the slope-aspect correction of multispectral scanner data. *Canadian Journal of Remote Sensing*, 8(2): 84–106.
Thiele, S. T., Grose, L., Samsu, A., Micklethwaite, S., Vollgger, S. A. and Cruden, A. R., 2017. Rapid, semi-automatic fracture and contact mapping for point clouds, images and geophysical data. *Solid Earth*, 8(6): 1241–1253.
Whitney, D. L. and Evans, B. W., 2010. Abbreviations for names of rock-forming minerals. *American Mineralogist*, 95(1): 185–187.
Ziph-Schatzberg, L., Wiggins, R., Woodman, P., Saleh, M., Nakanishi, K., Soletsky, P., Goldstein, N., Fox, M. and Tannian, B., 2018. *Compact visible to extended-SWIR hyperspectral sensor for unmanned aircraft systems (UAS). SPIE 10644 (Algorithms and Technologies for Multispectral, Hyperspectral, and Ultraspectral Imagery XXIV)*, article 106441G. 14 pages. DOI: https://doi.org/10.1117/12.2305615

Résumé

L'étude traditionnelle des tranchées paléosismiques, impliquant l'enregistrement des coupes et l'interprétation stratigraphique et structurelle, peut prendre beaucoup de temps et être entachée de biais et d'inexactitudes. Pour surmonter ces limites, une nouvelle méthodologie est présentée, intégrant des données photogrammétriques et hyperspectrales infrarouges en appui aux observations paléosismiques de terrain. Comme étude de cas, cette méthode est appliquée à deux tranchées paléosismiques creusées à travers un escarpement de faille post-glaciaire dans le nord de la Laponie finlandaise. L'imagerie hyperspectrale (HSI) est corrigée géométriquement et radiométriquement, traitée à l'aide d'algorithmes classiques de traitement d'images et d'apprentissage machine, et recalée sur un nuage de points photogrammétrique. Les modèles virtuels d'affleurements améliorés par HSI constituent un complément utile aux études paléosismiques de terrain, car ils fournissent non seulement une visualisation intuitive de l'affleurement et une archive de données facile d'emploi, mais permettent également une évaluation non biaisée de la composition minéralogique d'unités lithologiques ainsi qu'une délimitation semi-automatique des contacts et des structures de déformation dans un environnement virtuel 3D.

Zusammenfassung

Die traditionelle Protokollierung und stratigraphische/strukturelle Interpretation paläoseismischer Gräben kann zeitaufwendig sein und durch Verzerrungen und Ungenauigkeiten beeinflusst werden. Um diese Einschränkungen zu überwinden, wird ein neuer Arbeitsablauf vorgestellt, der hyperspektrale und photogrammetrische Daten integriert, um feldbasierte paläoseismische Beobachtungen zu unterstützen. Als Fallstudie wird diese Methode auf zwei paläoseismischen Gräben angewendet, die über eine postglaziale Verwerfung im nördlichen finnischen Lappland angelegt wurden. Das hyperspektrale Bild wird geometrisch und radiometrisch korrigiert, mit etablierten Bildverarbeitungsalgorithmen und maschinellen Lernverfahren verarbeitet und mit einer fotogrammetrischen Punktwolke verknüpft. Hyperspektrale Aufschlussmodelle sind eine sinnvolle Ergänzung zu paläoseismischen Feldstudien, da sie nicht nur eine intuitive Visualisierung des Aufschlusses ermöglichen und ein vielseitiges Datenarchiv darstellen, sondern auch erlauben, die mineralogische Zusammensetzung lithologischer Einheiten zu ermitteln sowie Kontakte und Deformationsstrukturen in einer virtuellen 3D-Umgebung zu analysieren.

Resumen

El estudio tradicional de las trincheras paleosísmicas, que implica la anotación, la interpretación estratigráfica y estructural, puede llevar mucho tiempo y verse afectado por sesgos e inexactitudes. Para

superar éste hándicap, se presenta un nuevo flujo de trabajo que integra datos hiperespectrales infrarrojos y fotogramétricos para apoyar las observaciones paleoseísmicas de campo. Como caso de estudio, este método se aplica en dos trincheras paleosísmicas excavadas a través de una cornisa post-glacial en el norte de la Laponia finlandesa. Las imágenes hiperespectrales (HSI) se corrigen geométrica y radiométricamente, se procesan utilizando algoritmos de procesamiento de imágenes establecidos y aproximaciones de aprendizaje automático, y se hacen corresponder sobre una nube de puntos derivada por fotogrametría. Los modelos de afloramiento virtual mejorados con HSI son un complemento útil para los estudios de campo paleosísmicos, ya que no solo proporcionan una visualización intuitiva del afloramiento y un archivo de datos versátil, sino que también permiten una evaluación imparcial de la composición mineralógica de las unidades litológicas y una delineación semiautomática de contactos y deformación en un entorno virtual 3D.

摘要

传统的古地震沟研究，包括测井、地层和构造解释，通常耗时并易受偏差和不准确性的影响。为了克服这些限制，本研究提出新的工作流程，整合红外高光谱和摄影测量数据，以辅助古地震的现场观测。本研究以芬兰拉普兰北部的冰川期后断层陡坡上开挖的两块古地震沟，作为研究案例。高光谱图像（*HSI*）经过几何和辐射校正，使用既有的图像处理算法和机器学习方法分析，并与由运动恢复结构所得点云进行配准。*HSI*增强的虚拟露头模型是古地震现场研究的有效补充，因为其不仅提供露头的直观可视化和多类型的数据存档，而且能够对岩性单元的矿物组成，在三维虚拟环境中进行无偏评估与半自动区分。